INVERSE CORE-RIM MICROSTRUCTURE IN (Ti,Ta)(C,N)-BASED CERMETS DEVELOPED BY A MECHANICALLY INDUCED SELF-SUSTAINING REACTION.

E. Chicardi*, J. M. Córdoba, M. J. Sayagués and F. J. Gotor

Instituto de Ciencia de Materiales de Sevilla (ICMS), CSIC-US, Américo Vespucio 49, 41092 Seville, Spain

ABSTRACT

Cermets with a nominal composition ($Ti_{0.8}Ta_{0.2}C_{0.5}N_{0.5}$ - 20 wt% Co) were synthesised by a mechanically induced self-sustaining reaction (MSR) process from stoichiometric elemental powder blends. The MSR allowed the production of a complex (Ti,Ta)(C,N) solid solution, which was the raw material used for the sintering process. The pressureless sintering process was performed at temperatures between 1400 ºC and 1600 ºC in an inert atmosphere. The microstructural characterisation showed a complex microstructure composed of a ceramic phase with an unusual inverse core-rim structure and a Ti-Ta-Co intermetallic phase that acted as the binder.

Keywords: mechanochemistry, combustion synthesis, cermet, inverse core-rim, carbonitride

*Corresponding Author. e-mail: ernesto.chicardi@icmse.csic.es Phone: +34 954 489217 Fax: +34 954 460665

INTRODUCTION

Titanium carbonitride-based cermets are replacing conventional cemented carbides and coated hard metals in cutting tools for some specific applications, such as in high-speed cutting due to better mechanical properties and chemical stability at high temperatures [1]. Cermets are composed of a hard ceramic phase, primarily a (Ti, Mt_1, Mt_2…)(C,N) solid solution, where Mt_1, Mt_2… are transition metals from the VB and VIB groups, and a metallic phase (usually Co or Ni) that acts as the binder. This combination of phases minimises the negative properties of ceramics and metals and allows the material to maximise useful properties, such as hardness, toughness, thermo shock resistance, high temperature creep resistance, high oxidation resistance, wear resistance, and plastic strain resistance, among others [2-5].

The physical and chemical properties of cermets can be adjusted for particular applications by introducing additives to the basic Ti(C,N)-Ni/Co system, which are typically other metal transition carbides [6]. For example, TaC is used when the hot hardness and the thermo shock resistance should be improved. Usually, several of these additives are added to cermets, and the typical core-rim structure is developed for the hard phase during the liquid phase sintering process. The core corresponds to the original undissolved Ti(C,N) particle; the rim is composed of a newly formed complex carbonitride solid solution produced through a dissolution/re-precipitation process during sintering, which contains Ti and others transition metals, such as Ta, Mo, W, V, or Nb [7-9].

The good cutting performance of cermets can be attributed to the mechanical behaviour of the rim phase, and therefore, many studies have focussed on changing the composition of this phase, i.e., the complex carbonitride solid solution, to improve the

mechanical properties and capacity of cermets [10]. This variation in composition is usually done by modifying the nature and amount of the binary carbides [11-14]. However, as the rim phase forms and grows during the liquid phase sintering process, the final composition depends strongly on the sintering temperature and the relative solubility of carbides in the binder phase, which makes the straightforward control of the rim stoichiometry difficult.

In 1976, Rudy [15] reported that the use of a carbonitride solid solution in the Ti-Mo-C-N and Ti-W-C-N systems as input material in the cermet production allows better control of the rim phase composition, and hence, cermets with superior thermal deformation, wear resistance and strength characteristics are obtained. Many other authors have since proposed the use of different complex solid solutions containing titanium and at least one element selected from the IVB, VB, and VIB groups as raw materials to fabricate cermets with improved properties and performance [6, 12, 16]. Moreover, other authors have stated that using these solid solutions as ceramic raw material could enable the production of cermets without a core-rim structure and, thus, maintain the mechanical behaviour of a rim-type composition and reduce the fracture paths that can generate along stressed core-rim interfaces. Currently, few studies have been published on the development of cermets without core-rim structures [17, 18].

Employing complex solid solution phases in cermet production is currently difficult because methods needed to synthesise the phases appropriately have not been developed. Usually, these solid solutions are obtained by reacting mixtures of metal carbides and nitrides that have been previously manufactured by a carbothermal reduction process from metal transition oxides at high temperatures and sometimes at high pressures [16, 19-21]. Subsequently, the material is crushed and ball-milled to

reduce the particle size, homogenised to the desired proportion of the binder phase, and processed by powder metallurgy techniques.

Córdoba et al. [22-24] have shown that the mechanochemical process denoted as a mechanically induced self-sustaining reaction (MSR) is an affordable and reproducible manufacturing process used to obtain complex transition metal carbonitrides. This reactive milling method uses the strong exothermic character of the carbide and nitride formation from the elements to obtain complex carbonitrides with high purity and with good control of stoichiometry. The same authors have also shown that this methodology may be successfully used in the development of cermets with the basic Ti(C,N)-Ni/Co composition [25].

In this study, a (Ti,Ta)(C,N) solid solution synthesised by the promising MSR method was employed as the ceramic raw material for cermet fabrication. The applied methodology for the powdered cermet synthesis consisted of performing one single milling process by adding the desired proportion of the binder component to the elemental mixture needed to generate the hard ceramic component by MSR in-situ. In this study, we focused on the evolution of the microstructure and chemical composition of the hard ceramic and binder phases during liquid phase sintering.

EXPERIMENTAL

Titanium powder (99% in purity, < 325 mesh, Strem Chemicals), tantalum powder (99.6% in purity, < 325 mesh, Alfa-Aesar), graphite powder (< 270 mesh, Fe ≤ 0.4%, Merck), and cobalt powder (99.8% in purity, < 100 mesh, Strem Chemicals) were used in this study. Tempered steel balls (15, d = 20 mm, m = 32.6 g) and 46.5 g of an elemental powder mixture were placed in a 300 ml tempered steel vial (67Rc) and milled under 6 atm of high-purity nitrogen gas (H_2O and $O_2 \leq 3$ ppm, Air Liquide)

using a modified planetary ball mill (Planetary Mill Pulverisette 4, Fritsch). The powder-to-ball mass ratio (PBR) was ~ 1/10.5, and a spinning rate of 400 rpm for both the rotation of the supporting disc and the superimposed rotation in the direction opposite to the vial was employed. The vial was purged with nitrogen gas several times, and the desired nitrogen pressure (6 atm) was selected before milling. The planetary mill allowed for operation at a constant gas pressure and the detection of self-propagating reactions during milling; this was possible by connecting the vial to a gas cylinder via a rotating union (model 1005-163-038, Deublin) and a flexible polyamide tube. The gas pressure was monitored continuously with a solenoid valve (model EVT307-5DO-01F-Q, SMC Co.) connected to a data acquisition system (ADAM-4000 series, Esis Pty Ltd.). When an MSR takes place, the temperature increase due to the exothermic reaction produces an instantaneous increase in the total pressure, and the ignition time can be obtained from the spike observed in the time-pressure data recorded.

Cermets were fabricated using a pressureless process. Powdered cermets were first shaped (green bodies) and then sintered at high temperatures. The shaping process was performed by uniaxial pressing at 2 tons for 5 min and cold isostatic pressing at 200 MPa for 10 min to yield cylinders of 13 mm in diameter and 9 mm in height. The green bodies were sintered at different temperatures from 1400 ºC to 1600 ºC for 60 min (heating and cooling rate 5 ºC/min) under an inert atmosphere (Argon gas, $H_2O \leq 8$ ppm and $O_2 \leq 2$ ppm, Linde) in a horizontal tubular furnace (IGM1360 model no. RTH-180-50-1H, AGNI). The Archimedes Method was used to measure the density of the sintered cermets.

X-ray diffraction diagrams of powders and polished surfaces of cermets were obtained with a Philips X'Pert Pro instrument equipped with a Θ/Θ goniometer using

Cu Kα radiation (40 kV, 40 mA), a secondary K_β filter, and an X'Celerator detector. The diffraction patterns were scanned from 20º to 140º (2Θ) in a step-scan mode at a step of 0.02º and a counting time of 275 s/step. The space group symmetry as well as the lattice parameters of $Ti_xTa_{1-x}C_yN_{1-y}$ and the binder phases were calculated from the whole set of peaks of the XRD diagram using the FULLPROF Suite software containing DICVOL, WinPLOTR, and FullProf computer programs [26]. The Williamson-Hall method [27] was used to separate the effects of domain size and microstrain on line broadening. The method assumes that the following mathematical relationship between the integral breadth (β), the size of the coherent crystalline domain (D), and the lattice distortion or microstrain (e) is applicable:

$$\frac{\beta \cos\theta}{\lambda} = \frac{1}{D} + 2e\left(\frac{2\sin\theta}{\lambda}\right)$$

A plot of $\beta \cos(\theta/\lambda)$ versus $2 \sin(\theta/\lambda)$ was constructed, and the microstrain and the domain size were obtained from the slope and the intercept, respectively.

The scanning electron microscopy (SEM) images were obtained on a Hitachi S-4800 SEM-Field Emission Gun microscope. The transmission electron microscopy (TEM) images and electron diffraction (ED) patterns were taken on a 200 kV Philips CM200 microscope equipped with a SuperTwin objective lens and a tungsten filament (point resolution ∅ = 0.25 nm). Powder samples were dispersed in ethanol, and droplets of the suspension were deposited onto a holey C film. For the TEM characterisation of consolidated cermets, thin disks (3 mm ∅) were prepared by a process of subsequent cutting, polishing, dimpling, and finally ion milling (DuoMiller, Gatan Inc. and ion miller model no. 1010, Fischione).

The transition metal content in the ceramic and binder phases was measured by energy dispersive X-ray spectrometry (EDX) with detectors coupled by the Hitachi scanning electron microscope and the Philips transmission electron microscope mentioned above. The overall carbon and nitrogen content in the cermets was determined by elemental analysis of C, N made by a LECO elemental analyser (mod. CNHS-932). Moreover, the total metal transition quantification was performed using an atomic emission spectrometer with an inductively coupled plasma (ICP) (mod. Ultima 2, Horiba Yobin Yvon).

RESULTS AND DISCUSSIONS

- Powder Synthesis.

A powder mixture of titanium, tantalum, graphite, and cobalt with an atomic ratio corresponding to a nominal composition of $Ti_{0.8}Ta_{0.2}C_{0.5}N_{0.5}$ + 20 wt% Co was ball-milled with nitrogen (6 bar). After 41.5 min of treatment in the planetary mill, a pressure spike was observed in the time-pressure data due to the occurrence of a highly exothermic reaction inside the vial (i.e., for the MSR process). This pressure spike was associated with the ignition of the self-sustaining reaction that led to the formation of a carbonitride ceramic phase, which was confirmed by XRD (Figure 1). The milling continued for 30 min after ignition to ensure the completion of the reaction and to obtain a narrow particle size distribution required to achieve an optimal cermet densification after sintering. This sample was labelled **P1**. A second sample with the same initial composition, labelled **P2,** was obtained under identical conditions, except that for this reference sample, the milling was stopped at the ignition (Table 1).

Figure 1 shows the XRD diagrams for the two powdered cermets obtained after the MSR process. Both diagrams were similar; the only difference was the presence of

less intense and broad reflections in the **P1** sample, which was due to the 30 min post-combustion milling that induced microstructural changes without any apparent chemical and crystallographic modification. The formation of a major phase that could be associated with a cubic phase and a ***Fm-3m*** space group was observed and confirmed by indexing with DICVOL06 software [26]. This phase was assigned to a complex titanium-tantalum carbonitride by comparing with the following reference diffraction patterns: TiN (38-1420), $TiC_{0.3}N_{0.7}$ (42-1488), $TiC_{0.7}N_{0.3}$ (42-1489), TiC (32-1383), TaC (35-0801) and TaN (49-1283). The XRD reflections appeared between the reflections corresponding to tantalum and titanium nitrides and carbides as observed in the inset in Figure 1, and therefore, this phase can be described as a $Ti_xTa_{1-x}C_yN_{1-y}$ solid solution. The existence of Ti, Ta, C, and N in the ceramic phase was determined by EDX and electron energy loss spectroscopy (EELS) measurements and confirmed the incorporation of nitrogen, which was incorporated from the working atmosphere into the final product during the MSR process.

Lattice parameter *a* of the cubic ceramic phase, which is dependent on the chemical composition of the solid solution, i.e., the atomic Ti/Ta and C/N ratios [28], was calculated using FullProf software. The crystalline domain size and lattice strain were also estimated by the Williamson-Hall equation. The value of these parameters (Table I) showed that the post-combustion milling reduced the crystalline domain size and increased the microstrain content in the sample but did not induce any noticeable crystallographic and chemical change as confirmed by the constant value observed in the lattice parameter. Moreover, the lattice parameter value was higher than those reported in previous studies for TiC_xN_{1-x} [29, 30] and is explained by the replacement of tantalum for titanium in the TiC_xN_{1-x} structure [22]. A small amount of unreacted

tantalum was also detected in the XRD diagrams, but no elemental titanium was observed.

The XRD diagrams in Figure 1 showed the presence of reflections that cannot be ascribed to elemental Co (binder), which was added to the Ti/Ta/C reactive mixture and can be considered inert in the self-sustaining reaction that produced the ceramic phase. It was possible to assign these reflections to intermetallic solid solutions in the Ti-Ta-Co ternary system, such as the $(Ta_xTi_{1-x})Co$ with cubic structure and ***Fd-3m*** space group as well as $(Ti_xTa_{1-x})Co_2$ with hexagonal structure and ***Pm-3m*** space group, using binary Ti-Co and Ta-Co phase diagrams [31], the Ti-Ta-Co ternary phase diagram at 950 ºC [32], and reference diffraction patterns for the Ti-Co and Ta-Co systems. These intermetallic phases were also produced during the MSR process triggered by the heat released during the carbonitride formation.

The morphology of **P1** and **P2** powdered cermets was characterised by SEM and representative images are shown in Figure 2. The **P1** sample showed the characteristic morphology of a material obtained by a dry milling process consisting of submicrometre particles forming irregular aggregates with an average size of 1 micron. Reference sample **P2** showed larger aggregates with a sintered appearance, of which some were in the millimetre range. This observation was a clear indication of the high local temperatures reached during the MSR and can also account for the appearance of the liquid phase and the formation of the intermetallic solid solution phases. These findings confirmed that the post-combustion milling was a necessary step to crush these large aggregates and homogenise the entire sample for the subsequent sintering process.

EDX compositional surface mapping was performed for the **P1** powdered cermet (Figure 3) to differentiate the ceramic and binder phases in the SEM images.

Cobalt was only found in the binder phase, was well distributed in the sample, and surrounded the ceramic particles. However, titanium and tantalum were found in both the ceramic and binder phases, which demonstrated the existence of an intermetallic solid solution in the binder. Figure 3 also showed that binder particles were significantly smaller than the ceramic particles. Furthermore, particles of unreacted tantalum were also found in some of the EDX maps, which confirmed the XRD results. A semi-quantitative study was performed by a punctual EDX-SEM analysis in ceramic particles and a ratio of Ta/Ti = 0.20 was determined, which was slightly below the nominal Ta/Ti ratio in the initial mixture (Ta/Ti = 0.25) (Table 1). The presence of unreacted Ta, and Ti and Ta in the binder phase was the origin of this compositional deviation. The same punctual EDX-SEM analysis could not be performed in the binder due to its small particle size.

The C and N contents in the ceramic phase were estimated from elemental analysis measurements assuming that the presence of C and N in the binder phase was negligible due to their low solubility in this phase [33, 34]; therefore, the quantification of C and N could be only attributed to the ceramic phase. A C/N ratio of 2.9 was determined (Table I), which was higher than the composition expected from the initial elemental mixture. The presence of Ti and Ta in the binder decreased the amount of these metals available to form the complex carbonitride, and consequently, a phase richer in carbon was obtained. The C/N and Ta/Ti quantifications allowed us to propose an average composition of the ceramic phase of $\mathbf{Ti_{0.83}Ta_{0.17}C_{0.74}N_{0.26}}$ for the **P1** sample. A similar stoichiometry was determined for the **P2** sample, which confirmed that the post-combustion milling did not produce any compositional variation.

- Pressureless Sintering

Cermets were prepared from **P1** powdered samples by pressureless sintering at temperatures between 1400 ºC and 1600 ºC. These cermets were labelled **C1-T,** where **T** corresponds to the sintering temperature. The density of the cermets as a function of sintering temperature is plotted in Figure 4. The relative density was calculated from the law of mixtures assuming the starting nominal composition ($Ti_{0.8}Ta_{0.2}C_{0.5}N_{0.5}$ + 20 wt% Co). The density increased with sintering temperature, which reached maximum value at 1550 ºC. The high temperatures needed for an optimal sintering were due to the presence of tantalum (m.p. = 3017 ºC) in the binder phase, which required high temperatures to obtain the liquid phase necessary to assist densification. The decrease observed at values above this temperature was attributed to the mass loss of binder due to an excessive fluidisation of the phase. The transition metal content in the cermets after sintering was confirmed by ICP, which provided evidence of the loss of Co at temperatures above 1550 ºC.

The XRD diagrams of **C1** cermets are shown in Figure 5, where the reflections of ceramic and binder phases are clearly observed. For all cermets, the $Ti_xTa_{1-x}C_yN_{1-y}$ reflections practically appeared at the same 2θ position, which suggested that the ceramic phase composition remained unchanged at the different sintering temperatures. However, the XRD reflections were displaced to higher diffraction angles when compared to the **P1** powdered sample (inset in Figure 5). The C/N ratio, which was measured by elemental analysis, was invariant between powdered and sintered cermets; therefore, the 2θ displacement was attributed to a different Ta/Ti ratio as a result of the titanium enrichment of the ceramic phase during the liquid phase sintering process.

Indexing of the XRD reflections corresponding to the binder phase showed the presence of the $(Ti_xTa_{1-x})Co_2$ hexagonal intermetallic solid solution between 1400 ºC and 1550 ºC. An electron diffraction (ED) study performed at the binder phase in the **C1-1550** sample confirmed the presence of this phase. In Figure 6, two ED patterns are shown along the [211] and [212] zone axis of this hexagonal structure. A semi-quantitative analysis by EDX confirmed that this phase was an intermetallic Ti-Ta-Co solid solution with a 1:2 stoichiometry.

Above the temperature of 1550 ºC, the XRD reflections were better allocated to intermetallic solid solutions with the same 1:2 stoichiometry $(Ti_xTa_{1-x})Co_2$ but with cubic structures (***Fd-3m*** space group). The Ti-Ta-Co ternary phase diagram [32] showed that both the hexagonal and cubic polymorphs had a very close composition interval with a fairly narrow coexistence region. Small compositional changes in the binder phase produced during the liquid phase sintering process can induce the presence of either of the two polymorphs in the cermet. The XRD diagram at 1500 ºC showed additional reflections (Figure 5) that were associated with the presence of a second intermetallic solid solution with a cubic structure (***Pm-3m*** space group) and a $(Ti_xTa_{1-x})Co$ stoichiometry in the cermet. Moreover, the estimated lattice parameter (a = 2.99 Å) for this cubic phase was very close to the binary TiCo compound (a = 2.986 Å).

The lattice parameters, domain crystalline sizes, and lattice strains for the $Ti_xTa_{1-x}C_yN_{1-y}$ ceramic phase and the $(Ti_xTa_{1-x})Co_2$ hexagonal and cubic phases are shown in Table 2. The lattice parameter *a* for the carbonitride phase showed a similar value for all sintering temperatures and were in agreement with the invariant 2θ position of the reflections in the XRD diagrams. The nanometric values for the crystalline size domains were inconsistent with the SEM and TEM observations (Figures 7 and 8), which showed micrometric ceramic particles. Thus, the large reflection broadening observed in

the XRD diagrams was not due to a size effect but to the existence of compositional fluctuations in the solid solutions that constitute the ceramic and binder phases, and they are produced during the dissolution/re-precipitation processes that occur during the liquid phase sintering process.

Characteristic SEM images of cermets are depicted in Figure 7. Cermets sintered at lower temperatures showed high porosity, poor wetting of the ceramic phase, and deficient distribution of the binder phase, which were all induced by the presence of Ta in the binder. The porosity decreased and the binder was homogeneously distributed in the cermet with increasing temperature. Concurrently, the smallest particles disappeared and the larger ones grew at the expense of the latter. Above 1550 ºC, all small particles were dissolved and the continuous growth of large ceramic particles was observed.

Most large particles in Figure 7 showed a core-rim structure that was typically formed by the dissolution/re-precipitation process during sintering [19]. These particles were characterised by a spherical core and a faceted rim. Several studies on the influence of the C/N ratio in TiC_xN_{1-x} particle morphology [7, 35] allowed us to suggest a higher N content in the core rather than in the rim. However, unlike what happens in particles with a classic core-rim structure, Figure 7 shows an inverse contrast between the core and rim; the rim exhibited a darker contrast, which suggested a composition richer in Ti. An inner rim with an even darker contrast was observed in some particles, and thus, its composition may be richer in titanium.

Bright field TEM images for the C1-1550 cermet are shown in Figure 8. Due to the transmission electron technique, the contrast was reversed compared to the SEM micrographs, and the ceramic particles appeared with a lighter contrast compared to the intermetallic binder. The ceramic phase clearly showed the inverse core-rim structure,

where the core exhibited a darker contrast manifesting a higher content in tantalum compared to the rim phase. This was in agreement with the SEM observations. As Figure 8 shows a ceramic particle with an inner rim and a very bright contrast (marked with an arrow); this was an indication of a higher titanium composition.

The electron diffraction (ED) studies were performed at the interface between the core and rim structures (round marked area), and the two ED patterns along the [011] and [-112] zone axes were found (inset in Figure 8). Both belonged to the same crystalline domain with a cubic structure and ***Fm-3m*** space group, which was in agreement with the XRD data. This demonstrated that the rim phase precipitated and grew onto the core while maintaining the same orientation and crystalline structure. Therefore, the only difference between the core and rim phases was the chemical composition.

The semi-quantitative EDX analyses were performed with the SEM equipment for all the cermets, and the results are shown in Figure 9. The cores exhibited the same Ti and Ta contents at different sintering temperatures and in relation with the ceramic phase of the **P1** precursor powder. Therefore, the core can be considered the undissolved ceramic particle during the sintering process. The rim phase also consisted of a $Ti_xTa_{1-x}C_yN_{1-y}$ solid solution but with a lower Ta/Ti ratio. In addition, this composition was almost constant with the temperature, which suggested that a similar level of saturation in Ta and Ti was reached in the binder phase. It was not possible to estimate the composition of the inner rim due to its small size compared to the electron probe.

A similar semi-quantitative EDX study was performed on the binder phase, and the results are shown in Figure 9. The high initial Ta/Ti ratio observed at 1400 ºC was

due to the incorporation of free Ta in the **P1** powdered sample into the binder phase and its homogenisation during sintering. The dissolution process of small ceramic particles became relevant with increasing temperature, although re-precipitation was also observed and was confirmed by the appearance of the core-rim structure in some of the ceramic particles. Thus, the Ta/Ti ratio decreased and reached a minimum value at 1500 ºC. At this temperature, most of the small particles had practically dissolved, which enriched the binder phase with Ti and induced the formation of a new intermetallic phase in the binder. At this temperature, the presence of two binder phases was observed with 1:2 and 1:1 stoichiometries, $(Ti_xTa_{1-x})Co_2$ hexagonal and $(Ti_xTa_{1-x})Co$ cubic, respectively. This last phase appeared in the SEM micrographs with a darker contrast (Figure 7c). Finally, above this temperature, the dissolution/re-precipitation process reached a steady state, the ceramic particles grew continuously and a constant Ta/Ti ratio was observed.

CONCLUSIONS

A titanium-tantalum carbonitride solid solution was employed as the raw ceramic material to fabricate cermets using Co as the binder phase instead of a mixture of different ceramic phases. This process was possible because of the mechanically induced self-sustaining reaction (MSR) method used to synthesise these complex carbonitrides. To simplify the synthetic method, the powdered cermets were obtained in a single milling process by adding the Co to the reactant mixture, which led to the carbonitride solid solution. Moreover, this raw material synthesised by the MSR contained a Ti-Ta-Co intermetallic solid solution instead of cobalt as the binder phase. After sintering, the formation of an ***inverse core-rim*** structure by a dissolution/re-precipitation process was confirmed, where the rim phase was richer in titanium than

the core. The dissolution of the smallest ceramic particles in the binder that already contained Ti and Ta caused the re-precipitation of the rim phase with higher titanium content.

Acknowledgments

This work was supported by the Spanish government under grant No. MAT2010-17046, which was financed in part by the European Regional Development Fund of 2007-2013. E. Chicardi and J. M. Córdoba were supported by the CSIC through JAE-Pre and JAE-Doc grants, respectively, which are financed in part by the European Social Fund (ESF).

REFERENCES

[1] Zhou SQ, Zhao W, Xiong WH. Microstructure and properties of cermets based on Ti(C,N). In: Salem J, Hilmas G, Fahrenholtz W, Ohji T, Wereszczak A, editors. Mechanical Properties and Processing of Ceramic Binary,Ternary, and Composite Systems2009. p. 41-50.

[2] Czura RJ. Cermets tackle tough jobs. Modern Machine Shop. 1989;62:66-74.

[3] Wick C. Cermet Cutting Tools. Manufacturing Engineering. 1987;99:35-40.

[4] Kolaska H. Cermets. Cutting materials with a future. Wire. 1990;40:343-6.

[5] Zhang S. Titanium carbonitride-based cermets: processes and properties. Materials Science and Engineering A. 1993;163:141-8.

[6] Ettmayer P, Kolaska H, Lengauer W, Dreyer K. Ti(C,N) Cermets - Metallurgy and properties. Int J Refract Met Hard Mater 1995;13:343-51.

[7] Qi F, Kang S. A study on microstructural changes in Ti(CN)-NbC-Ni cermets. Materials Science and Engineering A. 1998;251:276-85.

[8] Jung J, Kang S. Effect of ultra-fine powders on the microstructure of Ti(CN)-xWC-Ni cermets. Acta Materialia. 2004;52:1379-86.

[9] Mari D, Bolognini S, Feusier G, Cutard T, Verdon C, Viatte T, et al. TiMoCN based cermets: Part I. Morphology and phase composition. Int J Refract Met Hard Mater 2003;21:37-46.

[10] Isobe KH, JP), Kitagawa, Nobuyuki (Hyogo, JP), Yamazaki, Isao (Hokkaido, JP). Titanium-based alloy. United States: Sumitomo Electric Industries, Ltd. (Osaka, JP),Hokkaido Sumiden Precision Industries, Ltd. (Sorachi-gun, JP); 1999.

[11] Xiong J, Guo Z, Shen B, Cao D. The effect of WC, Mo2C, TaC content on the microstructure and properties of ultra-fine TiC0.7N0.3 cermet. Materials & Design. 2007;28:1689-94.

[12] Kwon WT, Park JS, Kim S-W, Kang S. Effect of WC and group IV carbides on the cutting performance of Ti(C,N) cermet tools. Int J Machine Tools and Manufacture. 2004;44:341-6.

[13] Zhang X, Liu N, Rong C. Microstructure and fracture toughness of TiC-ZrC-WC-Mo-Ni cermets. Int J Refract Met Hard Mater 2008;26:346-56.

[14] Kim S, Min KH, Kang S. Rim Structure in Ti(C0.7N0.3)-WC-Ni Cermets. J American Ceramic Society. 2003;86:1761-6.

[15] Rudy E. Spinodal carbonitride alloys for tool and wear applications. United States1976.

[16] Jin YZ, Liu Y, Wang YK, Ye JW. Synthesis of ultrafine (Ti, W, Mo, V)(C, N)-Ni composite powders by low-energy milling and subsequent carbothermal reduction-nitridation reaction. J Alloys and Compounds. 2009;486:L34-L6.

[17] Park S, Kang S. Toughened ultra-fine (Ti,W)(CN)-Ni cermets. Scripta Materialia. 2005;52:129-33.

[18] Kim YK, Shim JH, Cho YW, Yang HS, Park JK. Mechanochemical synthesis of nanocomposite powder for ultrafine (Ti, Mo)C-Ni cermet without core-rim structure. Int J Refract Met Hard Mater 2004;22:193-6.

[19] Andrén HO. Microstructure development during sintering and heat-treatment of cemented carbides and cermets. Materials Chemistry and Physics. 2001;67:209-13.

[20] Chen L, Lengauer W, Dreyer K. Advances in modern nitrogen-containing hardmetals and cermets. Int J Refract Met Hard Mater 2000;18:153-61.

[21] Liu Y, Jin Y, Yu H, Ye J. Ultrafine (Ti, M)(C, N)-based cermets with optimal mechanical properties. Int J Refract Met Hard Mater 2011;29:104-7.

[22] Cordoba JM, Aviles MA, Sayagues MJ, Alcala MD, Gotor FJ. Synthesis of complex carbonitride powders TiyMT1-yCxN1-x (M-T: Zr, V, Ta, Hf) via a mechanically induced self-sustaining reaction. J Alloys and Compounds. 2009;482:349-55.

[23] Cordoba JM, Sayagues MJ, Alcala MD, Gotor FJ. Monophasic nanostructured powders of niobium, tantalum, and hafnium carbonitrides synthesized by a mechanically induced self-propagating reaction. J American Ceramic Society. 2007;90:381-7.

[24] Córdoba JM, Sayagués MJ, Alcalá MD, Gotor FJ. Monophasic TiyNb1 - YCxN1 - x nanopowders obtained at room temperature by MSR. J Materials Chemistry. 2007;17:650-3.

[25] Cordoba JM, Alcala MD, Aviles MA, Sayagues MJ, Gotor FJ. New production of TiCxN1-x-based cermets by one step mechanically induced self-sustaining reaction: Powder synthesis and pressureless sintering. J European Ceramic Society. 2008;28:2085-98.
[26] Rodriguez-Carvajal J. FULLPROF. 2010.
[27] Williamson GK, Hall WH. X-ray line broadening from filed aluminium and wolfram. Acta Metallurgica. 1953;1:22-31.
[28] Park S, Kang YJ, Kwon HJ, Kang S. Synthesis of (Ti, M1, M2)(CN)-Ni nanocrystalline powders. Int J Refract Met Hard Mater 2006;24:115-21.
[29] Borrell A, Fernández A, Torrecillas R, Córdoba JM, Avilés MA, Gotor FJ. Spark plasma sintering of ultrafine TiCxN1-x powders synthesized by a mechanically induced self-sustaining reaction. J American Ceramic Society. 2010;93:2252-6.
[30] Cardinal S, Malchère A, Garnier V, Fantozzi G. Microstructure and mechanical properties of TiC-TiN based cermets for tools application. Int J Refract Met Hard Mater 2009;27:521-7.
[31] Baker H OH. Alloy phase diagrams: ASM Handbook; 1992.
[32] Xu H, Xiong X, Du Y, Wang P, Hu B, He Y. Phase equilibria of the Co-Ta-Ti system at 950 °C. Journal of Alloys and Compounds. 2009;485:249-54.
[33] Raghavan V. Co-Fe-N (cobalt-iron-nitrogen). J Phase Equilibria. 1993;14:623-4.
[34] Gabriel A, Chatillon C, Ansara I. Thermochemical and phase diagram analysis of the Ni-C, Co-C, and Co-Ni-C systems. High temperature science. 1988;25:17-54.
[35] Fukuhara M, Mitani H. Effect of nitrogen content on grain growth in Ti(C,N)-Ni-Mo sintered alloy. Powder Metallurgy International. 1982;14:196-200.

FIGURE CAPTIONS

Figure 1. X-ray powder diffraction diagrams of products obtained via the MSR process for samples **P1** and **P2**. (●) $Ti_xTa_{1-x}C_yN_{1-y}$; (□) Ta; (–) Cubic $(Ti_xTa_{1-x})Co$; (β) Hexagonal $(Ti_xTa_{1-x})Co_2$.

Figure 2. SEM micrographs showing (a) the morphology of **P1** powdered cermet and (b) the aggregates with sintered aspect observed in sample **P2**.

Figure 3. EDX-SEM map of **P1** powdered cermet showing the distribution of transition metals in the ceramic and binder phases. (Ti, red; Ta, green; Co, blue).

Figure 4. Density of cermets after pressureless sintering at different temperatures.

Figure 5. X-ray powder diffraction diagrams of cermets sintered at different temperatures. (●) $Ti_xTa_{1-x}C_yN_{1-y}$; (○) Cubic $(Ti_xTa_{1-x})Co$; (β) Hexagonal $(Ti_xTa_{1-x})Co_2$; (♦) Cubic $(Ti_xTa_{1-x})Co_2$.

Figure 6. Bright-field TEM images corresponding to cermet **C1-1550** and ED patterns along the [211] and [212], which correspond to the $(Ti_xTa_{1-x})Co_2$ hexagonal binder phase in the marked zone.

Figure 7. SEM micrographs of **C1** cermets sintered at different temperatures.

Figure 8. Bright-field TEM images corresponding to cermet **C1-1550** and ED patterns along the [011] and [-112], which correspond to the $Ti_xTa_{1-x}C_yN_{1-y}$ ceramic phase in the marked zone and in the interface between the core and rim.

Figure 9. Tantalum and titanium contents in the ceramic and binder phases of cermets sintered at different temperatures determined by EDX analysis. The results are expressed as Ta/Ti atomic ratio.

Table I. Ignition time and total milling time for powdered cermets synthesised by the MSR. Some parameters corresponding to the $Ti_xTa_{1-x}C_yN_{1-y}$ solid solution in **P1** and **P2** samples are shown.

	Sample	
	P1	P2
Ignition time (min)	41.5	41.5
Total milling time (min)	71.5	41.5
Lattice parameter (Å)	4.340	4.340
Crystalline domain size (nm)	29	61
Lattice microstrain (%)	0.29	0.13
Ta/Ti ratio by EDX	0.20	0.21
C/N ratio by elemental analysis	2.9	2.9

Table II. Lattice parameters, diffracting domain size (D) and microstrain (e) of ceramic and binder phases of cermets sintered at different temperatures.

	Ceramic phase				Intermetallic Phase				
Specimen	a (Å)	V (Å^3)	D (nm)	e % (x10e^6)	a (Å)	c (Å)	V (Å^3)	D (nm)	e % (x10e^5)
C1-1400	4.323	80.8	49	2.93	4.753	7.761	150.3	83	6.33
C1-1450	4.322	80.7	53	4.76	4.765	7.751	151.9	83	6.42
C1-1500	4.327	81.0	69	5.58	4.765	7.766	156.2	70	4.23
C1-1550	4.326	81.0	70	6.02	4.755	7.753	151.9	73	4.55
C1-1575	4.322	80.7	73	6.36	6.730	-	304.9	77	5.01
C1-1600	4.328	81.1	75	7.22	6.710	-	302.1	80	6.25

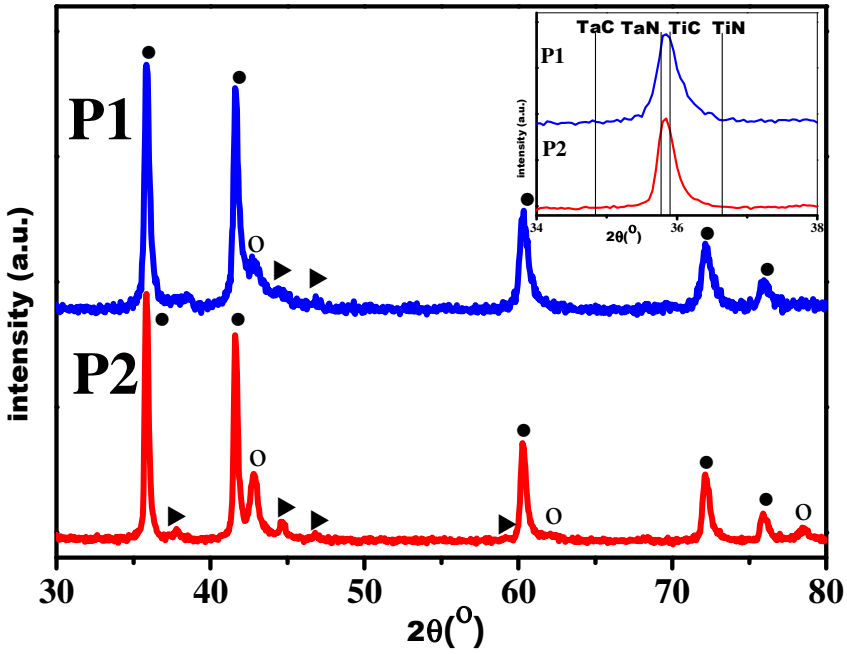

Figure 1. X-ray powder diffraction diagrams of products obtained via the MSR process for samples **P1** and **P2**. (●) $Ti_xTa_{1-x}C_yN_{1-y}$; (□) Ta; (–) Cubic $(Ti_xTa_{1-x})Co$; (β) Hexagonal $(Ti_xTa_{1-x})Co_2$.

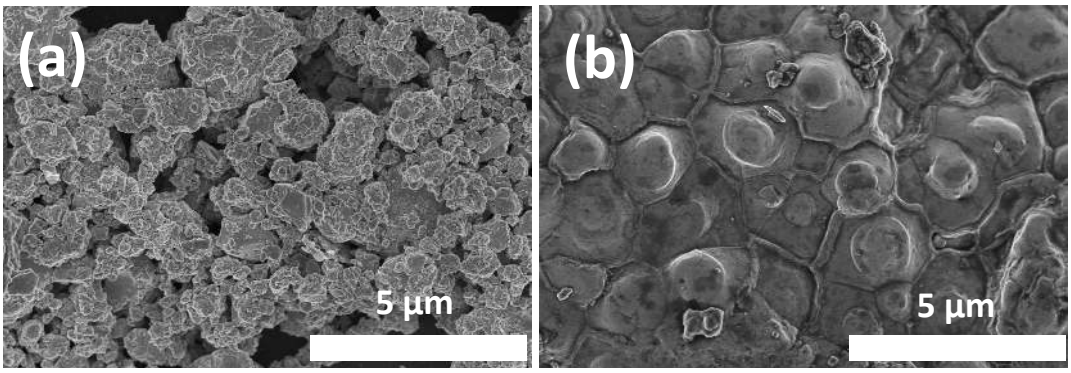

Figure 2. SEM micrographs showing (a) the morphology of **P1** powdered cermet and (b) the aggregates with sintered aspect observed in sample **P2**.

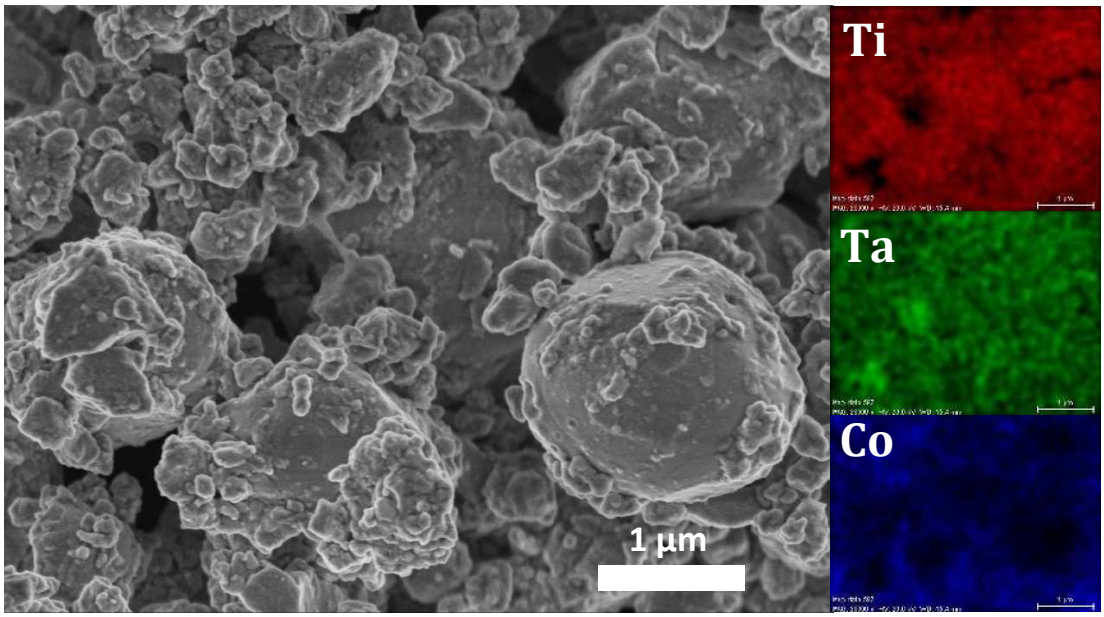

Figure 3. EDX-SEM map of **P1** powdered cermet showing the distribution of transition metals in the ceramic and binder phases. (Ti, red; Ta, green; Co, blue).

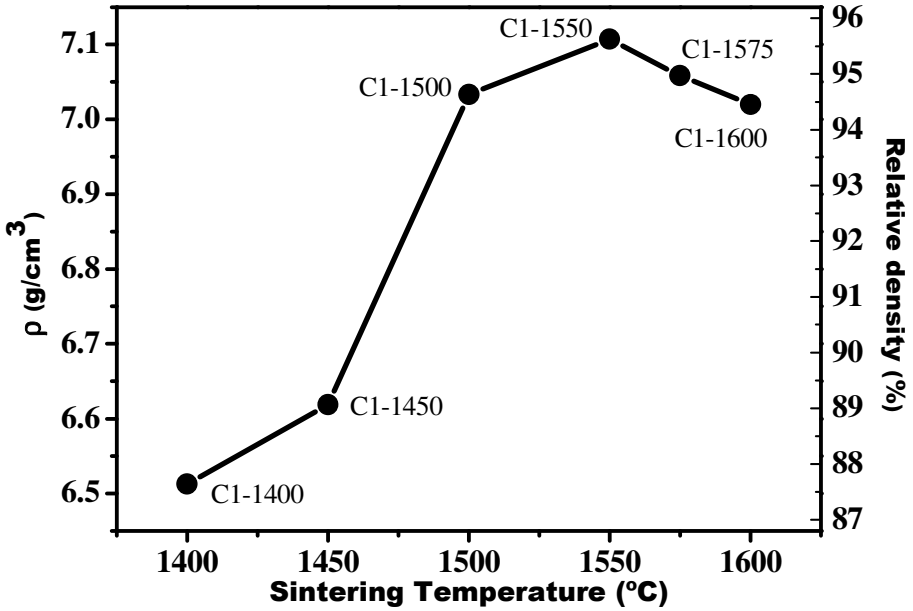

Figure 4. Density of cermets after pressureless sintering at different temperatures.

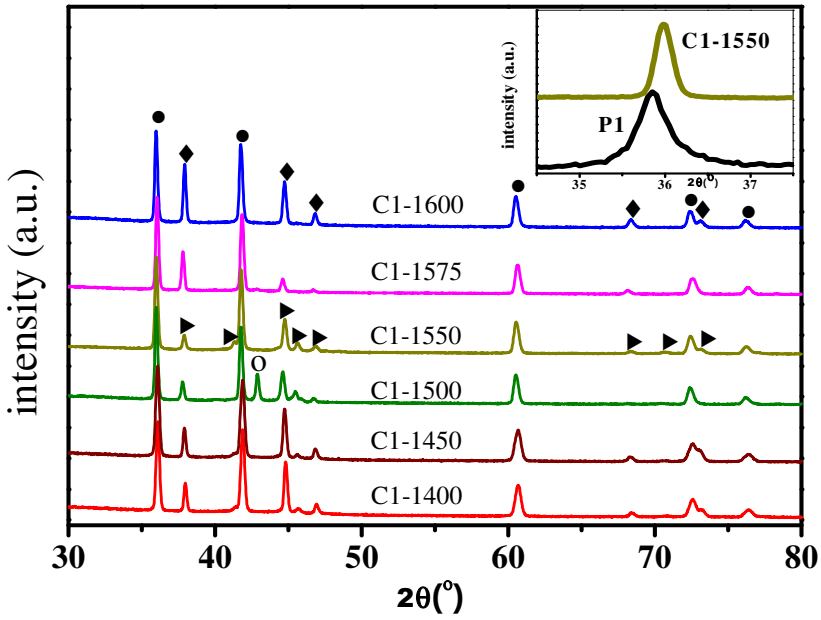

Figure 5. X-ray powder diffraction diagrams of cermets sintered at different temperatures. (●) $Ti_xTa_{1-x}C_yN_{1-y}$; (○) Cubic $(Ti_xTa_{1-x})Co$; (β) Hexagonal $(Ti_xTa_{1-x})Co_2$; (♦) Cubic $(Ti_xTa_{1-x})Co_2$.

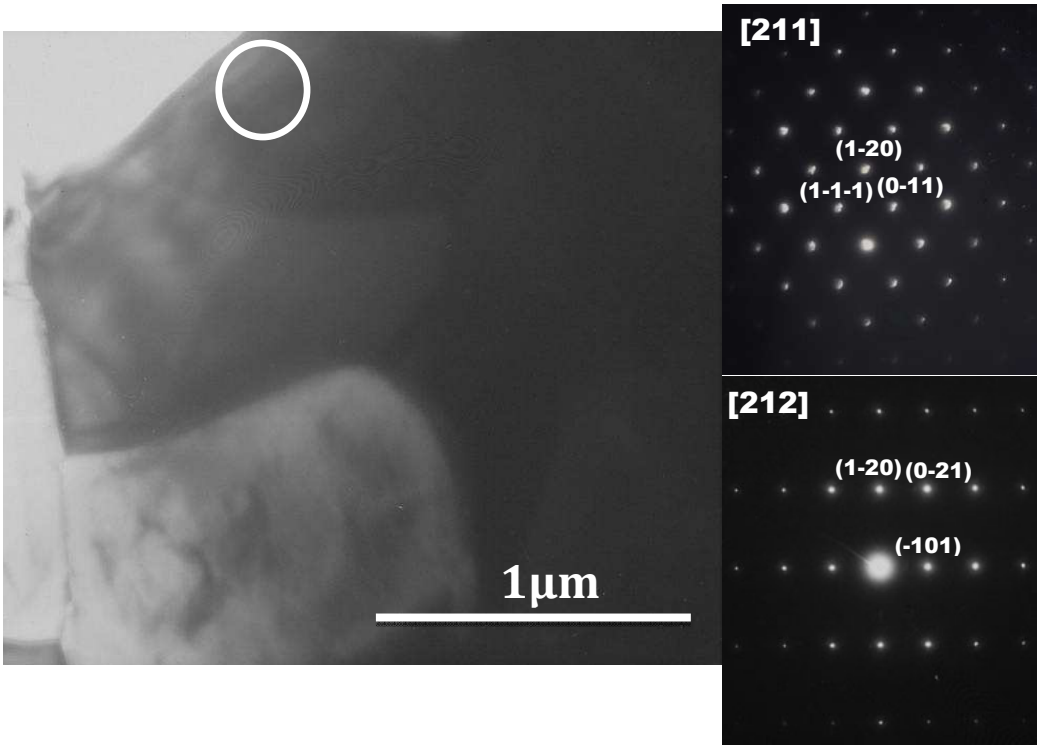

Figure 6. Bright-field TEM images corresponding to cermet **C1-1550** and ED patterns along the [211] and [212], which correspond to the $(Ti_xTa_{1-x})Co_2$ hexagonal binder phase in the marked zone.

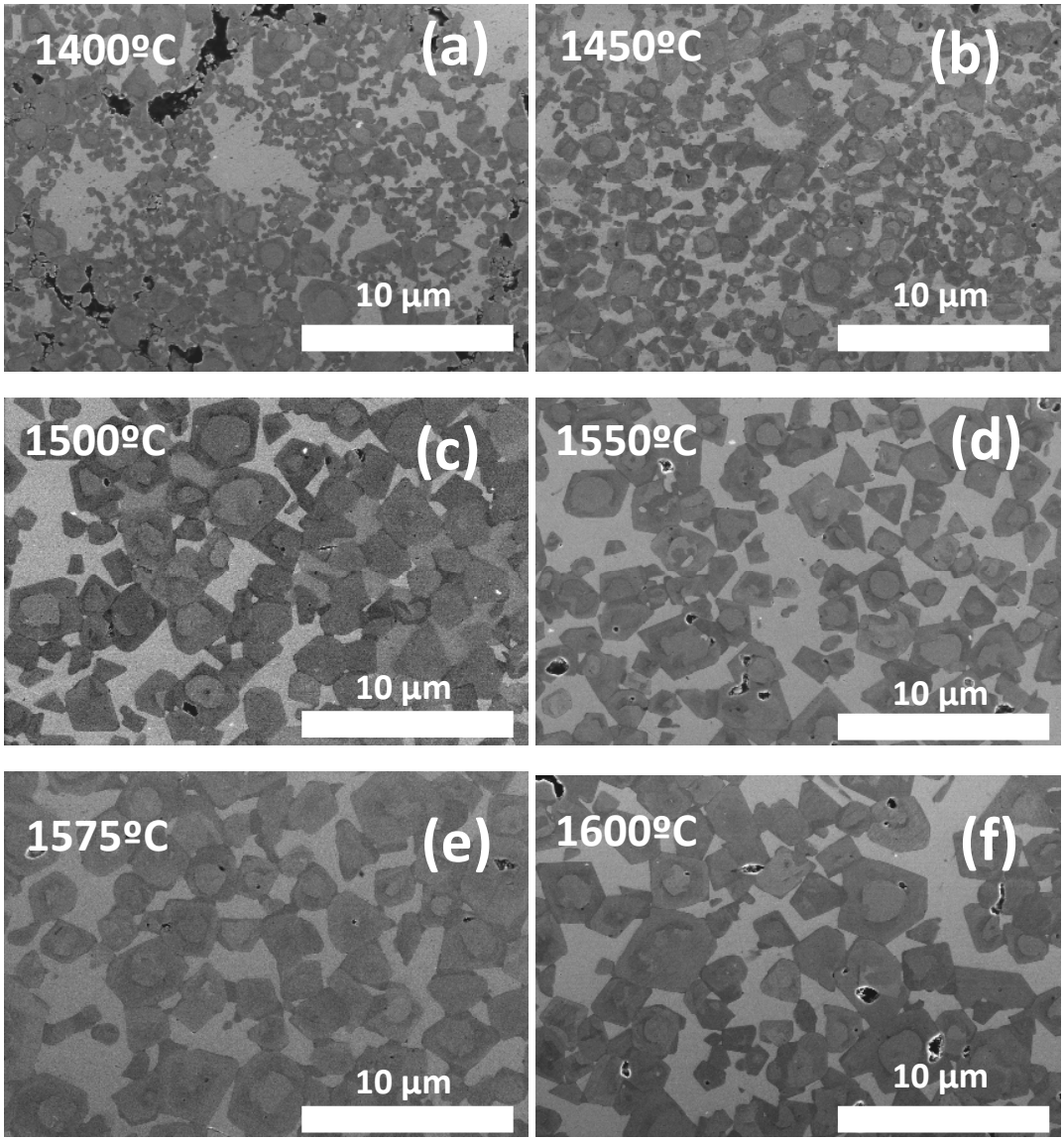

Figure 7. SEM micrographs of **C1** cermets sintered at different temperatures.

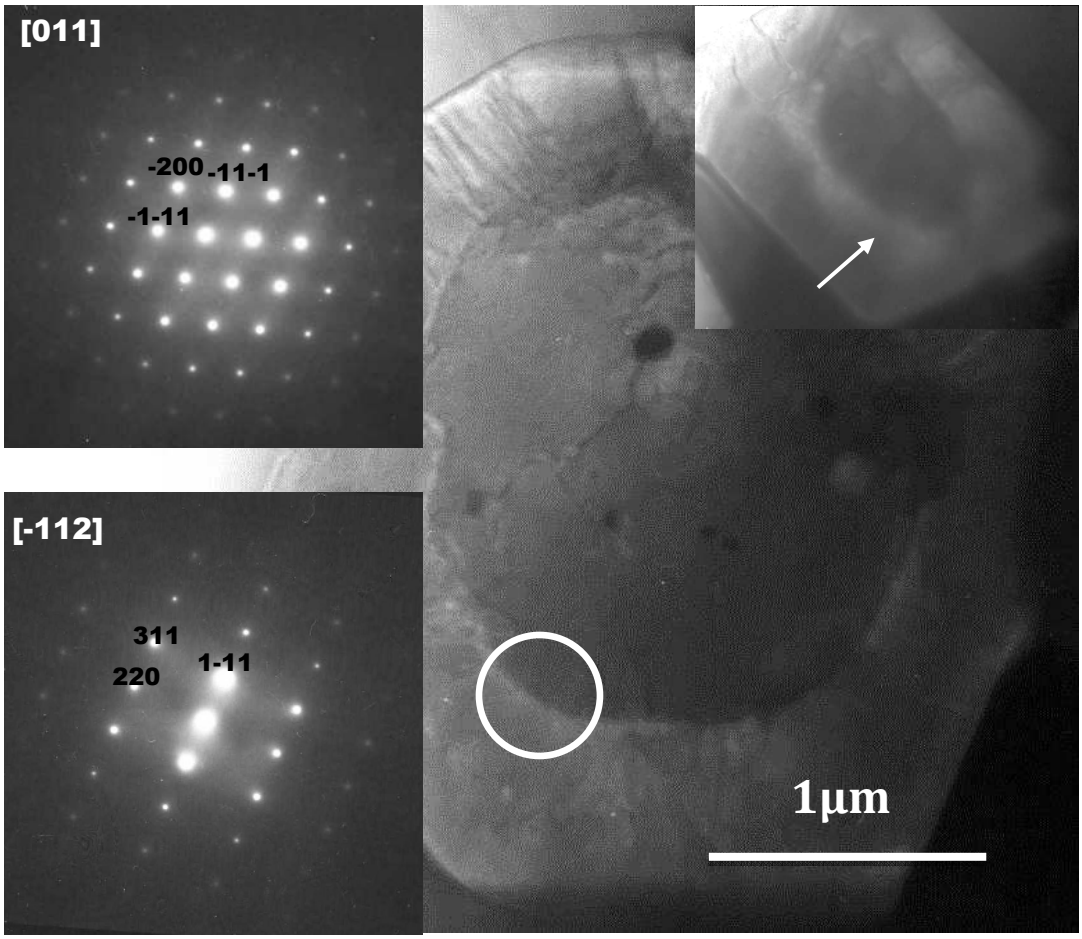

Figure 8. Bright-field TEM images corresponding to cermet **C1-1550** and ED patterns along the [011] and [-112], which correspond to the $Ti_xTa_{1-x}C_yN_{1-y}$ ceramic phase in the marked zone and in the interface between the core and rim.

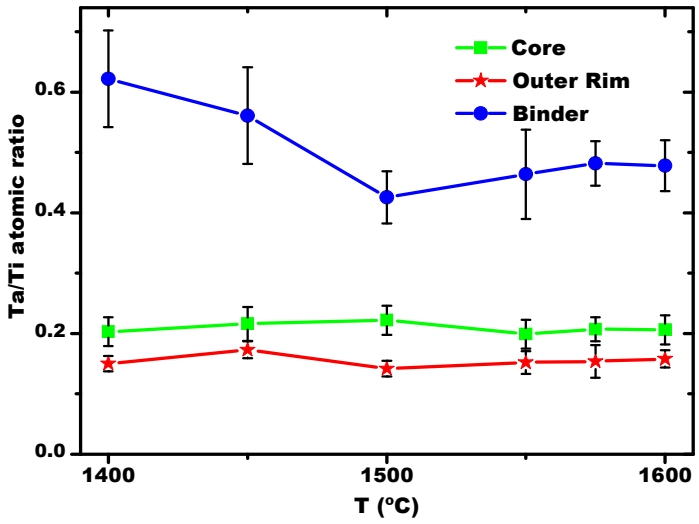

Figure 9. Tantalum and titanium contents in the ceramic and binder phases of cermets sintered at different temperatures determined by EDX analysis. The results are expressed as Ta/Ti atomic ratio.